J. Fluid Mech. (2012), *vol.* 704, *pp.* 61–88.
doi:10.1017/jfm.2012.214

The effect of an upstream hull on a propeller in reverse rotation

A. Verma, H. Jang and K. Mahesh†

Department of Aerospace Engineering and Mechanics, University of Minnesota, Minneapolis, MN 55455, USA

(Received 30 January 2012; revised 15 March 2012; accepted 30 April 2012; first published online 2 July 2012)

Propeller crashback is an off-design operating condition where a propeller rotates in the reverse direction. Experiments (Bridges 2004, *Tech Rep.* MSSU-ASE-04-1, Department of Aerospace Engineering, Mississippi State University) have shown that the presence of an upstream hull significantly increases the side force on a propeller in crashback below an advance ratio of $J = -0.7$. Large-eddy simulation (LES) is performed for a propeller with and without a hull at two advance ratios, $J = -1.0$ and $J = -0.5$. LES reproduces the experimentally observed behaviour and shows good quantitative agreement. Time-averaged flow fields are investigated for a qualitative understanding of the complex flow resulting from the interaction of the upstream hull with the propeller blades. At $J = -1.0$, two noticeable flow features are found for the case with the hull – a recirculation zone upstream in the vicinity of the propeller and a vortex ring much closer to the propeller. In contrast, at $J = -0.5$, there is a much smaller recirculation zone which is further upstream due to the increased reverse flow. As a result, the hull does not make much difference in the immediate vicinity of the propeller at $J = -0.5$. For both advance ratios, side force is mainly generated from the leading-edge separation on the suction side. However, high levels of side force are also generated from trailing-edge separation on the suction side at $J = -1.0$.

Key words: computational methods, flow–structure interactions, turbulence simulation, vortex interactions

1. Introduction

A forward moving marine vessel is decelerated by rotating the propeller in reverse. This off-design operating condition where the vessel moves in the forward direction while the propeller rotates in the reverse direction is termed crashback. Flow around the propeller in crashback is characterized by large-scale unsteadiness and separation. Low-frequency, high-amplitude off-axis forces and moments produced by this unsteadiness are transmitted to the vessel, inhibiting its ability to manoeuvre. Furthermore, the unsteady, separated flow near the control surfaces can reduce the effectiveness of the control surfaces.

The crashback condition is dominated by the interaction of the free-stream flow with the strong reverse flow from reverse propeller rotation (figure 1*a*). This interaction forms an unsteady vortex ring around the propeller and is the most remarkable aspect of the flow during crashback. The vortex ring state (VRS) is also an important

† Email address for correspondence: mahesh@aem.umn.edu

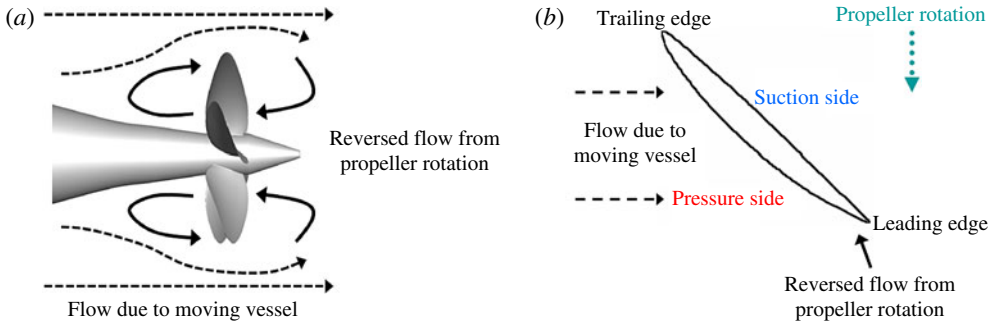

FIGURE 1. (Colour online) Crashback: (*a*) flow schematic; (*b*) location of leading and trailing edges, and pressure and suction sides on a blade section.

topological feature in helicopter aerodynamics, particularly a helicopter rotor in axial descending flight. Analogously to marine vessels, helicopters in VRS may experience loss of altitude, changed control surface effectiveness and low-frequency pitch and roll oscillations (Green, Gillies & Brown 2005).

Jiang *et al.* (1997) studied the structure of the unsteady vortex ring using particle image velocimetry (PIV) measurements. They noted that the asymmetry in the strength and location of the unsteady vortex ring is related to unsteady shaft forces and that the oscillation frequency of the vortex ring is much lower than the propeller rotation rate. Jessup *et al.* (2004) presented more detailed measurements of flow velocity fields using PIV and laser Doppler velocimetry (LDV).

Computational prediction of the flow around marine propellers has been performed using unsteady Reynolds-averaged Navier–Stokes equations (RANS) by Davoudzadeh *et al.* (1997) and Chen & Stern (1999). They showed that RANS yielded good results for forward ($U > 0$, $n > 0$) and backing ($U < 0$, $n < 0$) modes (attached-flow regime) but produced significant discrepancies in crashback ($U > 0$, $n < 0$) and crashahead ($U < 0$, $n > 0$) modes (separated flow regime). Here U denotes the velocity of the marine vessel and n denotes the rotational speed of the propeller.

A cylindrical cross-section of a propeller blade resembles an aerofoil. In the crashback condition, the leading and trailing edges of propeller blades exchange their roles. Hence, what used to be the sharp trailing edge in the forward operating condition becomes the leading edge in crashback and vice-versa. The leading (LE) and trailing edges (TE) of the propeller blades are defined as follows. LE is the downstream edge of the blade which first sees the reverse flow due to propeller rotation and TE is the other end as shown in figure 1(*b*). The large flow separation at the sharp leading edge may cause high-amplitude fluctuation of unsteady loads.

Mahesh, Constantinescu & Moin (2004) developed a non-dissipative and robust finite-volume method for LES on unstructured grids. Vyšohlid & Mahesh (2006) performed numerical simulations of a propeller in crashback with the same method at an advance ratio of $J = -0.7$. They showed that LES could yield good agreement for mean and r.m.s. values of unsteady loads. The computed power spectral density (PSD) for unsteady loads showed the same peak as the experiment at 5 rev^{-1}. Chang *et al.* (2008) performed LES at other advance ratios, $J = -0.5$ and $J = -1.0$, with the same LES code and computational grid as Vyšohlid & Mahesh (2006). They investigated instantaneous flow fields for a high thrust event and a low thrust event to understand the physics of crashback. They reported that a bi-modal behaviour with

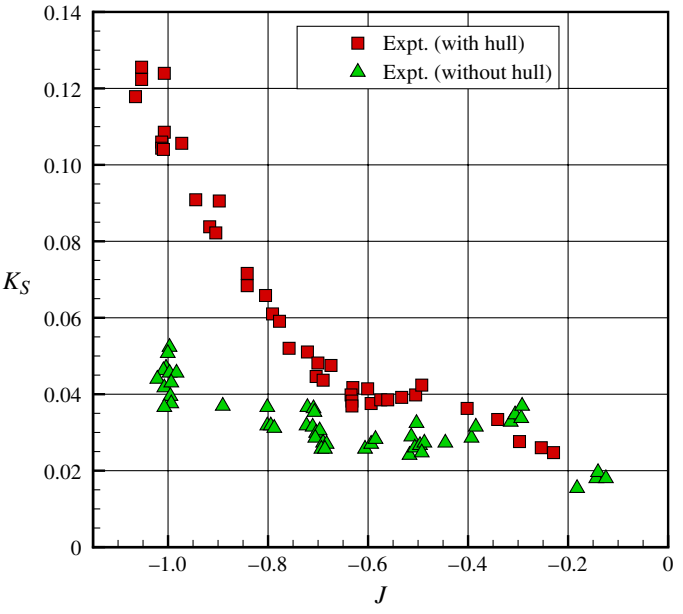

FIGURE 2. (Colour online) Increase in side-force magnitude with a hull compared to without a hull below $J = -0.7$ (Jessup *et al.* 2006).

vortex ring and axial jet modes occurred at low negative J. They also used the LES surface forces to predict shear stress and bending moments on the blades and obtained good agreement with experiments. Jang & Mahesh (2012) introduced two quantities to describe pressure contributions to thrust and side force and observed that most of the thrust and side force originated from the suction side of the leading edge of the propeller blades.

In the present work, flow past a propeller attached to an upstream hull, operating in the crashback condition is considered. A schematic of the flow is shown in figure 1; flow is from left to right. The inflow to the propeller is not the free stream but the wake of the hull. Bridges' experiment (Bridges 2004) on an open propeller with an upstream submarine hull in a large cavitation channel (LCC) noted that the side force increased dramatically below an advance ratio of $J = -0.7$ compared to Jessup's experiment (see Jessup, Fry & Donnelly 2006) without the hull in a 36 in. water tunnel (WT) (figure 2). However the reason for this discrepancy that an upstream hull causes is not well-understood. The objectives of the present work are to: (i) evaluate the ability of LES to predict the interaction of an upstream hull with the propeller, and (ii) provide a physical explanation for the above-mentioned experimental observation.

The paper is organized as follows. The set-up of the simulation, including the numerical method, grid and boundary conditions, is given in § 2. Results are shown for the effect of an upstream hull on a propeller at two advance ratios $J = -1.0$ and $J = -0.5$ in § 3. A physical mechanism to explain the results is summarized in § 4.

2. Simulation details

2.1. *Numerical method*

In LES, large scales are directly accounted for by the spatially filtered Navier–Stokes equations, whereas the small scales have to be modelled. Simulations are performed

in a frame of reference that rotates with the propeller. The spatially filtered incompressible Navier–Stokes equations in a rotating frame of reference are formulated for the absolute velocity vector in the inertial frame as follows:

$$\frac{\partial \overline{u}_i}{\partial t} + \frac{\partial}{\partial x_j}(\overline{u}_i\overline{u}_j - \overline{u}_i\epsilon_{jkl}\omega_k x_l) = -\frac{\partial \overline{p}}{\partial x_i} - \epsilon_{ijk}\omega_j\overline{u}_k + \nu\frac{\partial^2\overline{u}_i}{\partial x_j\partial x_j} - \frac{\partial \tau_{ij}}{\partial x_j}, \tag{2.1a}$$

$$\frac{\partial \overline{u}_i}{\partial x_i} = 0, \tag{2.1b}$$

where u_i is the inertial velocity in the inertial frame, p is the pressure, x_i are coordinates in the rotating non-inertial reference frame, ω_j is the angular velocity of the rotating frame of reference, ν is the kinematic viscosity, ϵ_{ijk} denotes the permutation tensor and the approximation $\overline{u_i\epsilon_{jkl}\omega_k x_l} \approx \overline{u}_i\epsilon_{jkl}\omega_k x_l$ is used. The overbar $\overline{(\cdot)}$ denotes the spatial filter and $\tau_{ij} = \overline{u_iu_j} - \overline{u}_i\overline{u}_j$ is the subgrid stress, which is modelled by using dynamic Smagorinsky model (Germano *et al.* 1991; Lilly 1992).

Equations (2.1) are solved by a numerical method developed by Mahesh *et al.* (2004) for incompressible flows on unstructured grids. The algorithm is derived to be robust without numerical dissipation. It is a finite-volume method where the Cartesian velocities and pressure are stored at the centroids of the cells and the face-normal velocities are stored independently at the centroids of the faces. A predictor–corrector approach is used. The predicted velocities at the control-volume centroids are first obtained and then interpolated to obtain the face-normal velocities. The predicted face-normal velocity is projected so that the continuity equation in (2.1) is discretely satisfied. This yields a Poisson equation for pressure which is solved iteratively using a multigrid approach. The pressure field is used to update the Cartesian control-volume velocities using a least-square formulation. Time advancement is performed using an implicit Crank–Nicolson scheme. The algorithm has been validated for a variety of problems over a range of Reynolds numbers (see Mahesh *et al.* 2004).

2.2. *Propeller geometry, computational mesh and boundary conditions*

Simulations are performed for a marine propeller DTMB 4381, which is a five-bladed, right-handed propeller with variable pitch, no skew and no rake. The propeller has been used in various experiments (Jiang *et al.* 1997; Jessup *et al.* 2004, 2006) and computations (Davoudzadeh *et al.* 1997; Chen & Stern 1999; Vyšohlid & Mahesh 2006; Chang *et al.* 2008; Jang & Mahesh 2012). For the hull geometry, a standard axisymmetric hull (DTMB Model 5495-3) is used. In the simulations, half of the hull body is used and stabilizing fins are ignored. Details of the propeller and hull geometry are given in Bridges (2004).

The computational domain is a cylinder with diameter $7.0D$ and length $14.0D$ where D is the diameter of the propeller disk. Free-stream velocity boundary conditions are specified at the inlet and the lateral boundaries. Convective boundary conditions are prescribed at the exit. Since the velocities in the governing equations (2.1) are referred to in the inertial frame, boundary conditions on solid walls are also prescribed in the inertial frame. Thus, boundary conditions on the rotor part, blades and hub are specified as $u = \omega \times r$, while those on that hull or shaft are prescribed as no-slip boundary conditions. A schematic of the computational domain and boundary conditions is shown in figure 3.

In the present work, simulations are performed for the propeller with and without a hull at two advance ratios, $J = -1.0$ and $J = -0.5$. The grid for the propeller without a hull has 7.7 million control volumes and with a hull, 7.3 million control volumes.

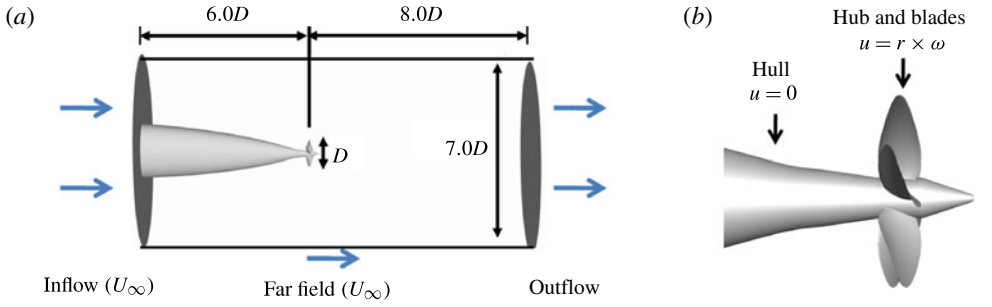

FIGURE 3. (Colour online) (*a*) Computational domain and boundary conditions on domain boundaries; (*b*) boundary conditions on solid walls.

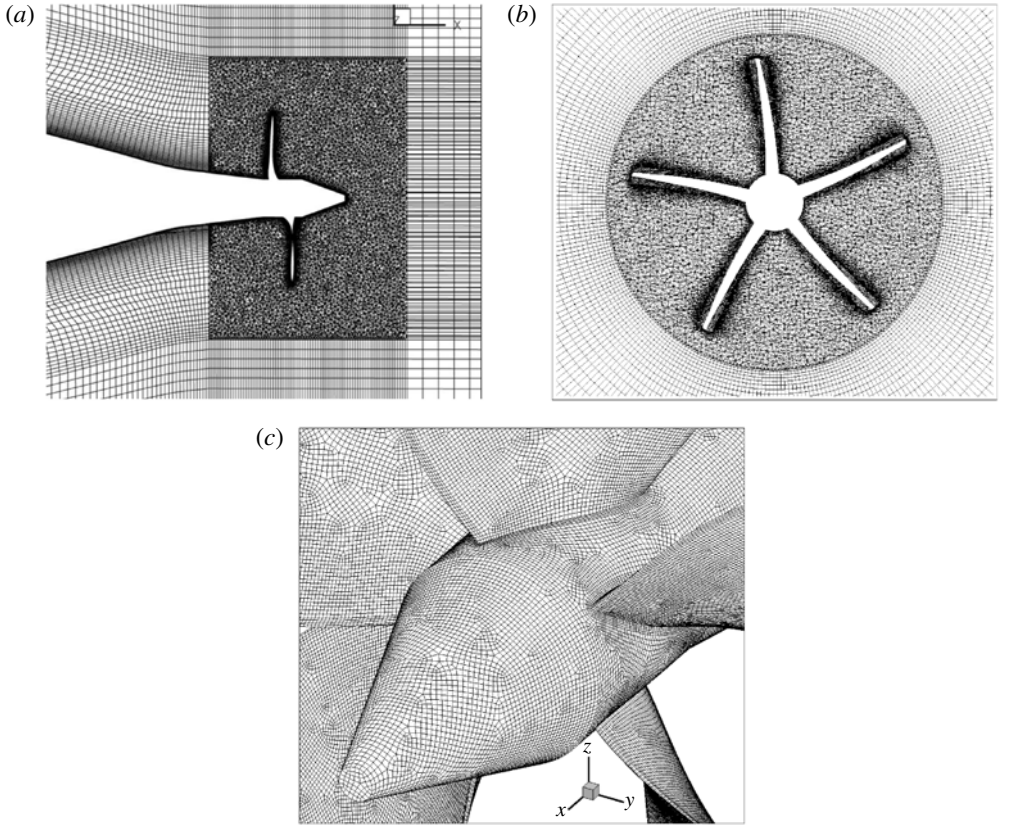

FIGURE 4. Computational grid: (*a*) x, y plane of the grid for the propeller with a hull; (*b*) $x = 0$ plane of the grid; (*c*) surface mesh.

The unstructured grid for the propeller with a hull is shown in figure 4. The surface of the propeller is meshed by quadrilateral elements. Four layers of prisms are extruded from the surface with a minimum wall-normal spacing of $0.0017D$ and a growth ratio of 1.05. A compact cylindrical region around the propeller is meshed with tetrahedral volumes while hexahedral volumes are used in the rest of the domain.

3. Results

Large-eddy simulations are performed under the crashback condition at two negative advance ratios and Reynolds number $Re = 480\,000$. The advance ratio J and Reynolds number Re are defined as

$$J = \frac{U}{nD}, \quad Re = \frac{UD}{\nu} \tag{3.1}$$

where U is the free-stream velocity, n is the propeller rotational speed, D is the diameter of the propeller disk and ν is kinematic viscosity.

The notation used throughout the paper is as follows. Thrust T is the axial component of force, torque Q is the axial component of the moment of force, and F_H and F_V denote the horizontal and vertical components of the force respectively. The vector sum of F_H and F_V is the projection of the force onto the direction perpendicular to the propeller axis and is termed the side force S. Since computations are performed in a rotating frame of reference, the side force is transformed to the inertial reference frame. The horizontal and vertical components of the side force, F_H and F_V, respectively, can be obtained from a rotational transformation using the angle between the rotating frame and the inertial frame.

Non-dimensional thrust coefficient K_T, torque coefficient K_Q and side-force magnitude coefficient K_S are given by

$$K_T = \frac{T}{\rho n^2 D^4}, \quad K_Q = \frac{Q}{\rho n^2 D^5}, \quad K_S = \frac{\sqrt{F_H^2 + F_V^2}}{\rho n^2 D^4} \tag{3.2}$$

where ρ is the density of the fluid. Henceforth, $\langle\cdot\rangle$ denotes the mean value and $\sigma(\cdot)$ denotes standard deviation. Root-mean-square (r.m.s.) of the side force is defined as

$$\sigma(K_F) = \tfrac{1}{2}(\sigma(K_H) + \sigma(K_V)) \tag{3.3}$$

where

$$K_H = \frac{F_H}{\rho n^2 D^4}, \quad K_V = \frac{F_V}{\rho n^2 D^4}. \tag{3.4}$$

Instead of using the advance ratio J, the experimental data of Bridges (2004) and Bridges, Donnelly & Park (2008) primarily use the similarity parameter η, defined as

$$\eta = \frac{n}{n_{sp}} \tag{3.5}$$

where n_{sp} is the propeller rotational speed for self–propulsion, which is the propeller speed at a given forward velocity such that the thrust produced by the propeller is equal to the drag of the vessel.

3.1. *Propeller without a hull at $J = -0.7$*

The validity of the current LES methodology for propeller crashback is established by the LES of propeller without a hull at $J = -0.7$ by Jang & Mahesh (2012) which is in good agreement with the experimental results of Jessup *et al.* (2004, 2006). Computed mean K_T and K_Q are located between the 36 in. WT and the open-water towing-tank (OW) results as shown in table 1. Figure 5 shows that the computed circumferentially averaged flow fields also compare favourably with those measured with LDV by Jessup *et al.* (2004). The blanked out zone is where the hull/shaft and the propeller blade would be. Jang & Mahesh (2012) also obtain frequency spectra of blade loads and time-averaged velocity profiles that are in good agreement with experiment.

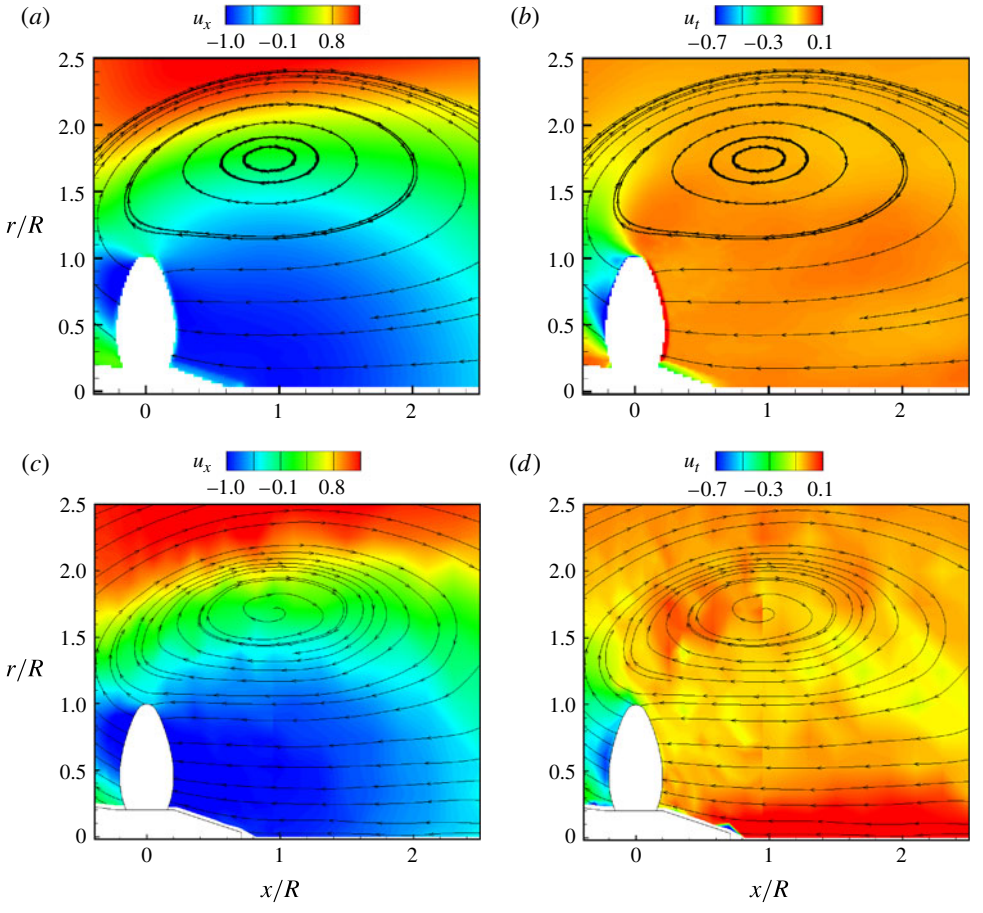

FIGURE 5. (Colour online) $J = -0.7$. Circumferentially averaged flow fields: (*a*) axial velocity and (*b*) tangential velocity (LES; Jang & Mahesh 2012); (*c*) axial velocity and (*d*) tangential velocity (experiment; Jessup *et al.* (2004)).

	$\langle K_T \rangle$	$\langle K_Q \rangle$	$\langle K_S \rangle$
LES Jang & Mahesh (2012)	−0.37	−0.074	0.023
WT Jessup *et al.* (2004)	−0.33	−0.065	0.024
OW Jessup *et al.* (2006)	−0.41	−0.078	

TABLE 1. $J = -0.7$: mean values of thrust, torque and side-force magnitude given by previous computation and experiments.

3.2. *Effect of a hull at* $J = -1.0$

In this subsection, the flow for a propeller with and without a hull at $J = -1.0$ is validated with available experimental data and then studied using time-averaged flow statistics. This is followed by a suggested physical mechanism to explain the occurrence of higher side force in the presence of the hull in § 3.3.

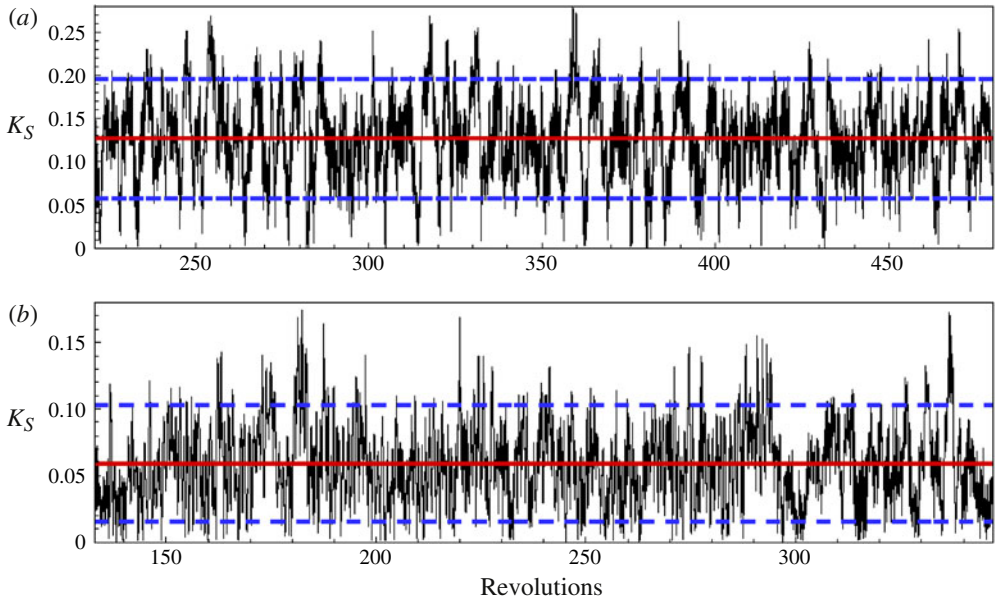

FIGURE 6. (Colour online) $J = -1.0$. Time history of unsteady loads on the propeller blades. ——, $\langle K_S \rangle$; – – – –, $\langle K_S \rangle \pm 1.5\sigma(K_S)$: (*a*) w/ hull, (*b*) w/o hull.

		$\langle K_S \rangle$	$\sigma(K_F)$	$\sigma(K_S)$
With hull	LES	0.126	0.095	0.046
	Bridges *et al.* (2008)	0.105–0.126	0.096–0.104	0.042–0.047
Without hull	LES	0.059	0.046	0.029
	Jessup *et al.* (2004)	0.036–0.052	—	0.022

TABLE 2. $J = -1.0$. Computed and experimental values of mean of side-force magnitude and r.m.s. of side force on the blades with and without a hull.

3.2.1. *Time history and spectra of loads*

The time history of K_S shown in figure 6 is over 259 propeller rotations for propeller with hull and 214 rotations without hull. The horizontal lines in figure 6 are the mean and the mean plus or minus 1.5 times the standard deviation. $K_S - \sigma(K_S)$ represents low side-force magnitude and $K_S + \sigma(K_S)$ represents high side-force magnitude. As shown in table 2, computed mean and r.m.s. of side force show agreement with the experimental results for propellers with and without a hull at $J = -1.0$. Very importantly, the LES predicts the experimentally observed increase in side force in the presence of the hull.

The frequency spectra of the loads are computed by dividing the time history into a finite number of segments with 50 % overlap, applying a Hann window for low aliasing and rescaling to maintain the input signal energy. Each such segment is then transformed into the frequency domain by taking a fast-Fourier transform (FFT). The PSD is then averaged over all the segments to provide a relatively smooth curve. Figure 7 shows the PSD of the coefficient of side-force magnitude K_S and horizontal force K_H with and without a hull. The most important peak is at $f = 5$ rev^{-1} which

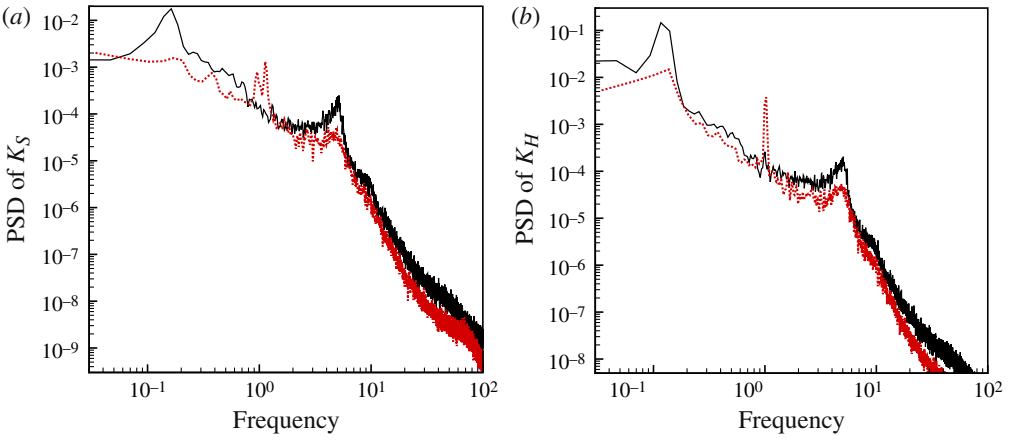

FIGURE 7. (Colour online) $J = -1.0$. PSD. ——, w/ hull; · · ·, w/o hull: (*a*) K_S, (*b*) K_H.

has also been observed by Vyšohlid & Mahesh (2006), Chang *et al.* (2008) and Jang & Mahesh (2012). This corresponds to the passage of the blades of the five-bladed propeller. Note that the magnitude of this peak is higher in the presence of the hull.

A low-frequency, high-amplitude modulation of the side force has important ramifications for the manoeuvrability of the vessel. For the K_S spectra in figure 7(*a*), there is a peak at a lower frequency of $f = 0.16$ rev^{-1} for the spectra with the hull. It must be noted that Bridges *et al.* (2008) report a non-dimensional frequency of peak propeller horizontal force at $\eta = -0.9$ to be $f \sim 0.12$ rev^{-1}. This agrees well with a low frequency of $f = 0.11$ rev^{-1} seen for K_H (figure 7*b*). Note that $\eta = -0.9$ in Bridges *et al.* (2008) approximately corresponds to $J = -1.0$. The corresponding low-frequency peak without the hull is at $f = 1$ rev^{-1}, in agreement with experiments (Jessup *et al.* 2004). Only the non-axial force quantities (K_H, K_V, K_S, $\tan^{-1}(F_V/F_H)$) exhibit these low frequencies as they are absent for K_T and K_Q (not shown here).

3.2.2. *Time-averaged flow field*

Time-averaged statistics of the flow field were computed over 170 propeller rotations for a propeller with a hull and 172 rotations without a hull, which is included in the time window for which the time history of K_S is shown. Figure 8 shows an x, y-plane slice cutting through the centre and along the length of the shaft/hull. Time-averaged pressure contours and velocity streamlines are plotted. Flow features distinguishing the presence of the hull are clearly observed. The velocity streamlines in figure 8 reveal a recirculation zone upstream of the blades in the presence of the hull. No such recirculation zone appears near the shaft without a hull. This region of high circulation is created by the interaction between the wake of the hull and reverse flow produced by propeller rotation. In the presence of the hull, the vortex ring appears to be more compact and its centre is closer to the blades compared to the more elongated and stretched vortex ring without the hull. The suction side of the blades with the hull sees lower levels of pressure than without the hull. Reverse rotation also causes reverse flow without the hull. However in this case, the flow interacts with a free stream which enters the propeller disk with higher momentum than the hull wake.

Figure 9 illustrates the effect of the hull on axial velocity in the y, z plane at the x-location $x/R = 0$. The perspective in these figures is such that the hull/shaft is going

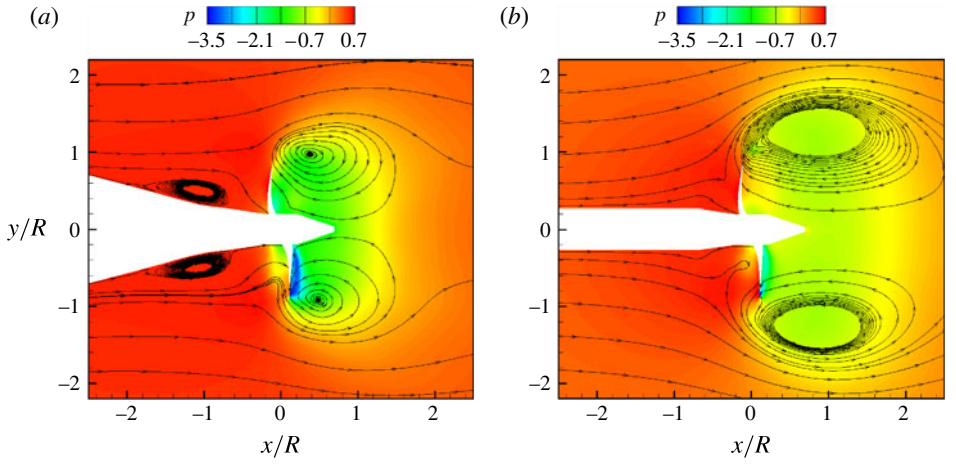

FIGURE 8. (Colour online) $J = -1.0$. Time-averaged pressure contours with streamlines: (*a*) w/ hull, (*b*) w/o hull.

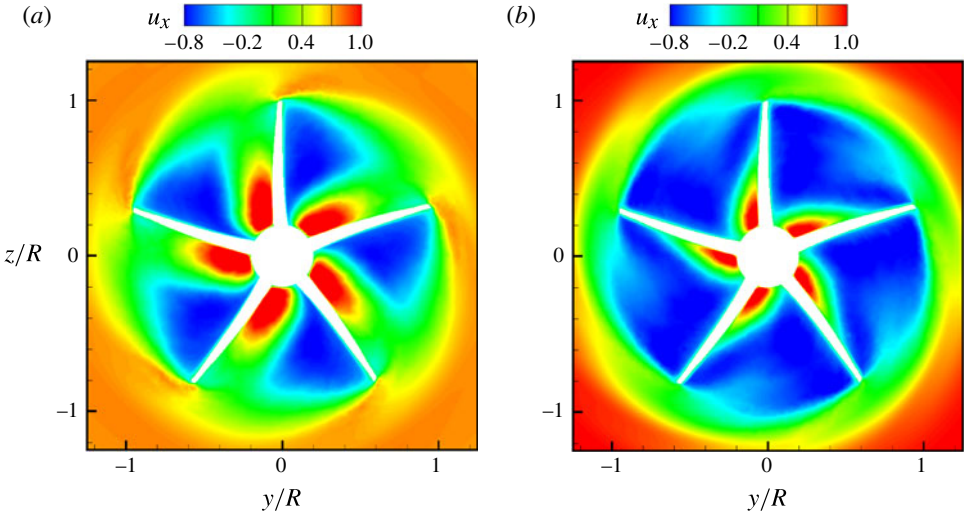

FIGURE 9. (Colour online) $J = -1.0$. Time-averaged axial velocity at $x/R = 0$: (*a*) w/ hull, (*b*) w/o hull.

into the plane of the paper and the free stream is coming out of the plane of the paper. It can be inferred that reverse flow decreases between the propeller blades with the hull but note that the velocity becomes higher near the root of the blades. This point will be reinforced in figure 11 in the next section.

3.2.3. *Circumferentially averaged flow field*

The time-averaged flow statistics are further averaged along lines of constant radius to yield circumferentially averaged statistics in the x, r plane. Figure 10 shows contours of axial velocity with streamlines with and without a hull. For the case with a hull, the upstream recirculation zone is nestled between the blades and the

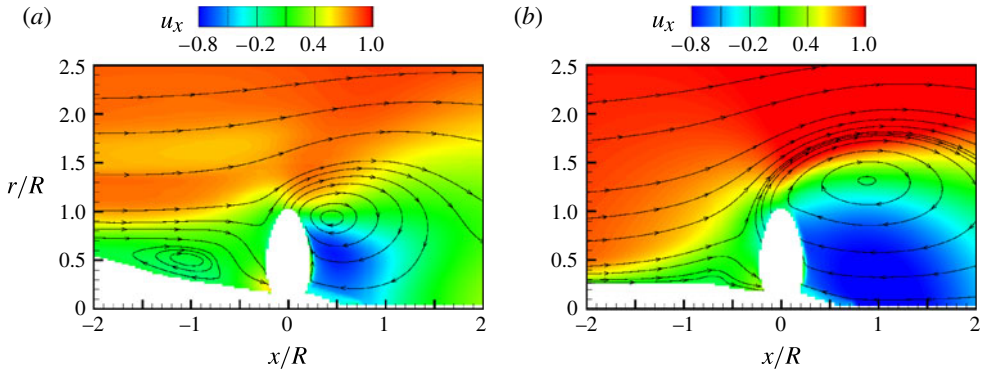

FIGURE 10. (Colour online) $J = -1.0$. Circumferentially averaged axial velocity with streamlines (*a*) w/ hull, (*b*) w/o hull.

	x_{cen}/R	r_{cen}/R
With hull	0.45	0.94
Without hull	0.88	1.32

TABLE 3. $J = -1.0$. Locations of centres of vortex rings with and without a hull from circumferentially averaged flow fields.

	d_{cen}/R
LES	1.04
Bridges (2004)	1.10

TABLE 4. $J = -1.0$. Distance of centre of vortex ring from the propeller centre from LES and from an experiment, both with a hull.

rising contours of the hull centred at the coordinates $(x/R, r/R) \equiv (-1.03, 0.51)$. Note that the vortex ring is much closer to the tip of the blade when the hull is present. The wake of the hull has lower streamwise momentum which causes the vortex ring to form closer to the blade when a hull is present. There is also increased reverse flow entering the propeller disk in the absence of a hull. Table 3 compares the locations of the centre of the vortex ring with and without the hull obtained using the current LES. The distances are measured relative to the propeller centre. Table 4 shows good agreement for the distance of the centre of the vortex ring between LES and experiment at $\eta = -0.9$ (see Bridges 2004).

Axial velocity profiles are extracted from six x-locations spanning one radius upstream to half a radius downstream of the blade. Figure 11 clearly shows the difference that the presence of a hull makes: the solid line is for the propeller with a hull while the dotted line is without a hull. Lower velocity is observed for $r/R > 1.4$ at all x-locations in the presence of the hull. This supports our assertion that lower momentum of the incoming upstream flow causes the centre of the vortex ring to be located closer to the blades with the hull. The first of these locations ($x/R = -1.0$) is close to the centre of the recirculation region ($x/R = -1.03$) in the simulation with a hull and the velocity profile at this location is shown in figure 11(*a*). The velocity

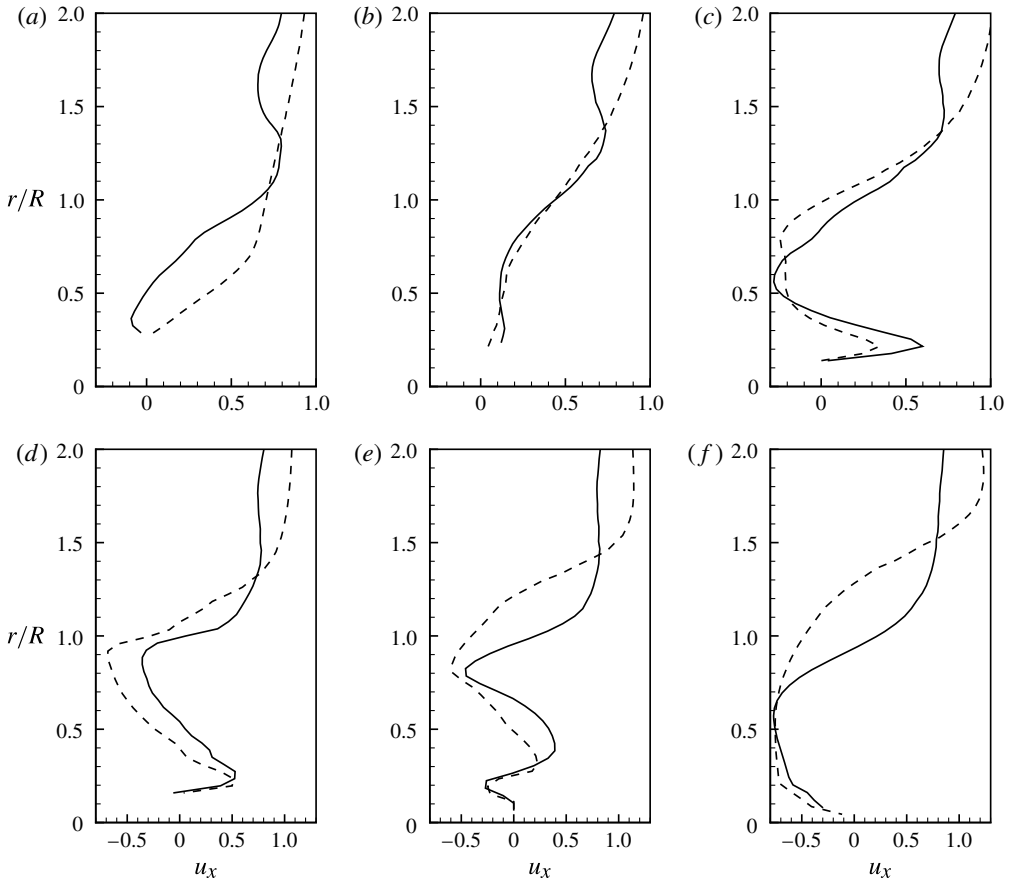

FIGURE 11. $J = -1.0$. Circumferentially averaged axial velocity profiles from six x-locations; ——, w/ hull; – – –, w/o hull; (*a*) $x/R = -1.0$, (*b*) $x/R = -0.5$, (*c*) $x/R = -0.2$, (*d*) $x/R = 0$, (*e*) $x/R = 0.2$, (*f*) $x/R = 0.45$.

profile with a hull clearly indicates a low-momentum velocity profile compared to a without hull, similar to that obtained behind a backward-facing step close to the centre of the primary vortex (see Le, Moin & Kim 1997). In fact, there is even a slight reverse velocity close to the hull body ($r/R < 0.5$). Not surprisingly, this is close to the centre of the recirculation zone. Figure 11(*c*) shows that in the near field of the trailing edge of the blade at ($x/R = -0.2$), the blade root ($r/R < 0.4$) sees a higher velocity with the hull. This is consistent with higher velocity near the blade root as seen in figure 9(*a*). Without the hull, figure 11(*d–f*) clearly shows increased reverse inflow from downstream into the propeller disk. The closer vortex ring is responsible for the rather high velocity gradient with the hull in figure 11(*e*) near $0.7 < r/R < 0.9$. The line plot for u_x at $x/R = 0.45$ shown in figure 11(*f*) passes through the centre of the vortex ring for the case with the hull.

Figure 12(*a*) shows smaller outward radial velocity near the tip of the blade with the hull, thus pulling the centre of the vortex ring closer to the blade. However, figure 12(*c*) shows that the radial velocity near the leading edge of the blade ($x/R = 0.2$) is much higher with a hull due to induction by the closer vortex ring. Figure 13 compares tangential velocity profiles with and without a hull. It is useful to

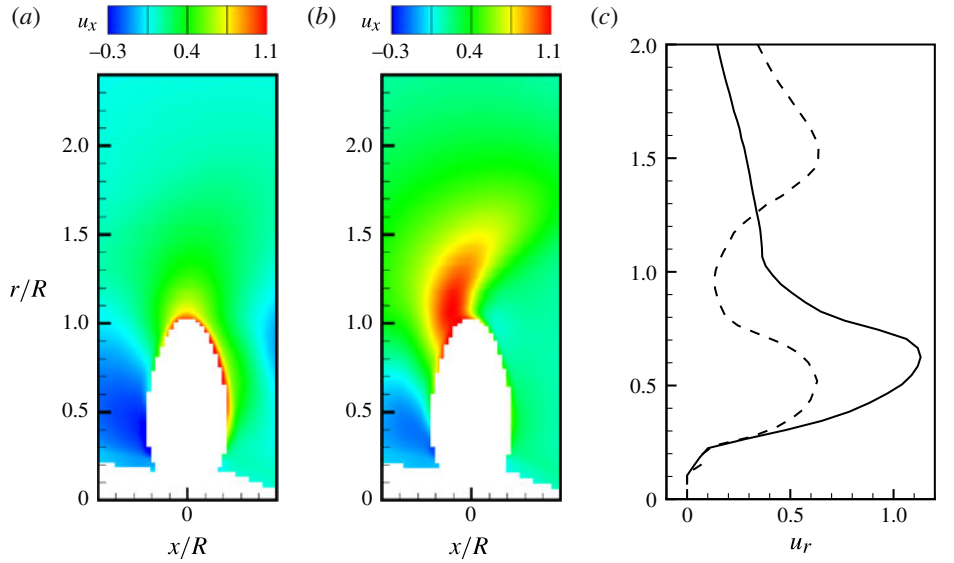

FIGURE 12. (Colour online) $J = -1.0$. Circumferentially averaged radial velocity. Contours (*a*) w/ hull, (*b*) w/o hull. (*c*) Profile at $x/R = 0.2$; – – –, w/ hull; ——, w/o hull.

note that the blade tangential velocity $u_\theta = \pi(r/R)/J$ at any radial section r/R on the blade surface. Mean u_θ is primarily negative due to the reverse propeller rotation in crashback. The tangential velocity is always higher in the presence of the hull within the blade passage ($x/R = 0$) and near the leading edge of the blades ($x/R = 0.2$). In figure 13(*b*), the slope of the solid line (w/hull), denoting u_θ, is almost π/J indicating that the flow tends to move along with the blade tangential velocity. It will be shown in § 3.3 that the leading edge of the blade (around $x/R = 0.2$) is a region of great flow separation. The swirl is so much higher with the hull that it persists even at a downstream distance of $x/R = 0.45$ whereas it is almost absent without a hull.

Turbulent kinetic energy (k) is a measure of three-dimensional unsteadiness and turbulence in the flow. Figure 14(*a,b*) shows k normalized by the maximum turbulent kinetic energy k_{max} in each case. With the hull, $k_{max} = 1.6$ whereas $k_{max} = 0.6$ without a hull. Hence, k is much higher in the presence of a hull. In figure 14(*a,b*), the solid line outlines where the propeller blade would be. It is observed that k is highest near the leading edge of the blades for both the cases, possibly related to the unsteadiness caused by the reverse flow separating at the sharp leading edge. There are two important effects of the hull worth mentioning (figure 14*a*). Firstly, k is relatively high in the near field of the blade ($0.2 < x/R < 0.5$) and this is directly attributable to greater unsteadiness stirred up by the closer unsteady vortex ring. Secondly, the distribution of k near the leading edge is highest in the outward half of the propeller blade ($r/R > 0.5$) compared to the inward half ($r/R < 0.5$) of the blade without a hull. This can be seen more clearly in the line plot of k obtained from the leading edge (figure 14*c*) where maximum k occurs near $r/R \sim 0.65$ with a hull and $r/R \sim 0.3$ without a hull. Also, the magnitude of this maximum k with a hull is almost three times that without a hull. Thus, it can be concluded that a greater peak velocity fluctuation acting through a greater moment arm must exert greater forces and moments on the propeller.

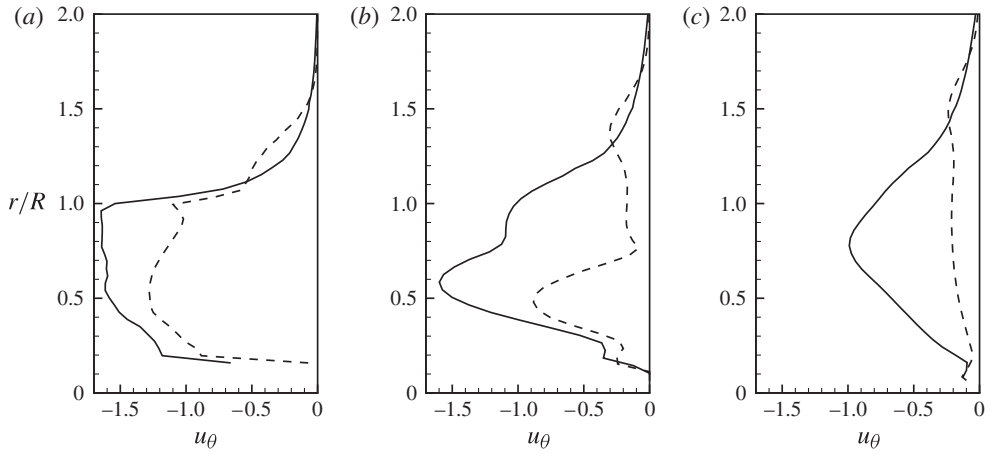

FIGURE 13. $J = -1.0$. Circumferentially averaged tangential velocity profiles from three x-locations; ——, w/ hull; – – –, w/o hull. (*a*) $x/R = 0$; (*b*) $x/R = 0.2$; (*c*) $x/R = 0.45$.

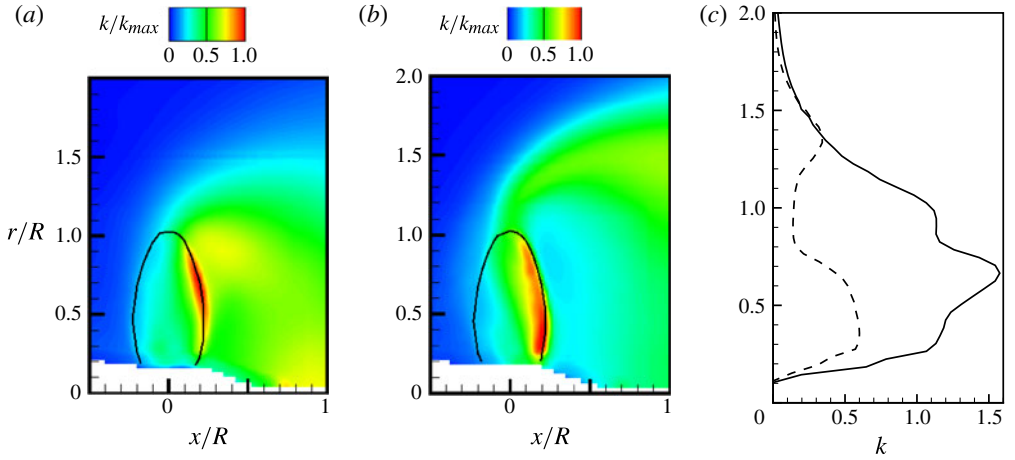

FIGURE 14. (Colour online) $J = -1.0$. Circumferentially averaged turbulent kinetic energy. Contours for k/k_{max}: (*a*) w/ hull, (*b*) w/o hull. (*c*) k profile at $x/R = 0.2$: ——, w/ hull; – – –, w/o hull.

3.2.4. *Propeller loads*

At high Reynolds numbers, viscous effects are smaller than pressure effects. Hence pressure force is the dominant term in blade loadings. Jang & Mahesh (2012) introduced a quantity to describe the pressure contribution to side-force magnitude (F_S) on a unit surface:

$$F_S = \sqrt{F_H^2 + F_V^2} = \sqrt{(\boldsymbol{F}\cdot\boldsymbol{j})^2 + (\boldsymbol{F}\cdot\boldsymbol{k})^2} = |p|\sqrt{(\boldsymbol{n}_f\cdot\boldsymbol{j})^2 + (\boldsymbol{n}_f\cdot\boldsymbol{k})^2} = |p|\beta_f, \quad (3.6)$$

where p is the pressure, $\boldsymbol{n}_f$ is the outward normal vector of the face, $\boldsymbol{j}$ and $\boldsymbol{k}$ are base unit vectors in the plane normal to the axial direction; β_f is invariant with rotation and hence compatible with our rotating system. $|p|\beta_f$ is the pressure contribution to

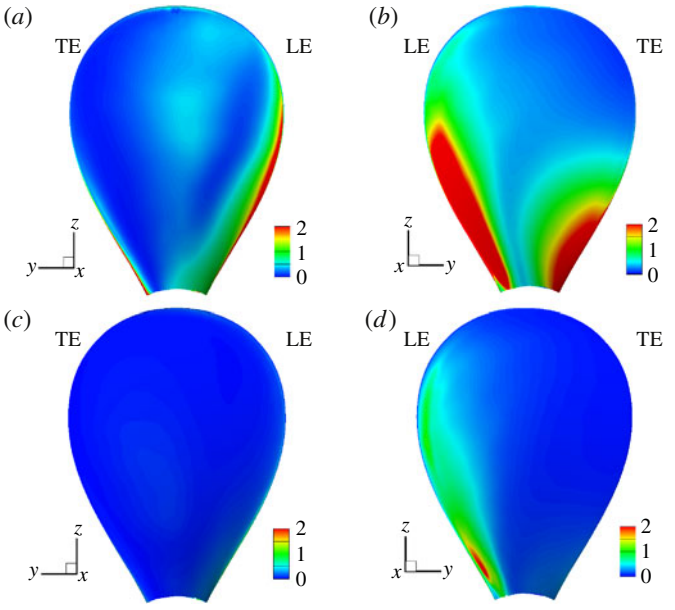

FIGURE 15. (Colour online) $J = -1.0$. Pressure contribution to side force on (*a*) pressure side w/ hull; (*b*) suction side w/ hull; (*c*) pressure side w/o hull; (*d*) suction side w/o hull.

side-force magnitude K_S and $\sigma(p)\beta_f$ is the pressure contribution to the r.m.s. of side force $\sigma(K_F)$.

The quantity $\sigma(p)\beta_f$ on the propeller blades is examined in figure 15 to reveal the location of generation of side force at $J = -1.0$. For clarification, the face of the propeller blade towards the incoming hull wake or free stream is the pressure side and the other face towards the reverse flow is the suction side. Figure 15 shows that the pressure contribution to side force is significantly higher with a hull. On the pressure side, a propeller with a hull (figure 15*a*) has higher $\sigma(p)\beta_f$ than without a hull (figure 15*c*), especially on the leading edge. The biggest pressure contribution to the side force, though, comes from the suction side. As had been observed by Jang & Mahesh (2012) at $J = -0.7$, the leading edge on the suction side is responsible for most side force without a hull (figure 15*d*). This observation can now also be extended to $J = -1.0$ with a hull (figure 15*b*). In fact, with a hull, even the trailing edge on the suction side shows a pressure contribution to the side force. A closer look at the trailing edge of the suction side reveals that most of the pressure contribution to the side force comes from near the blade root.

The above observations are reinforced more quantitatively in figure 16. The blade surface is divided into ten constant-radius sections. The mean side-force magnitude experienced by these ten sections on both the pressure and suction sides of the blade are plotted as histograms. The force is averaged over 59 rotations for the propeller with a hull and 55 rotations without a hull. Note the higher relative magnitude of K_S for the case with a hull (figure 16*a*) than without a hull (figure 16*b*). For both cases, the pressure side generates less side force than the suction side. Most of the side force is generated from close to the blade root without a hull. However, with the hull, the blade area up to $r/R = 0.4$ is responsible for high side-force magnitude. This blade-root-ward trend in the radial location of generation of high side force

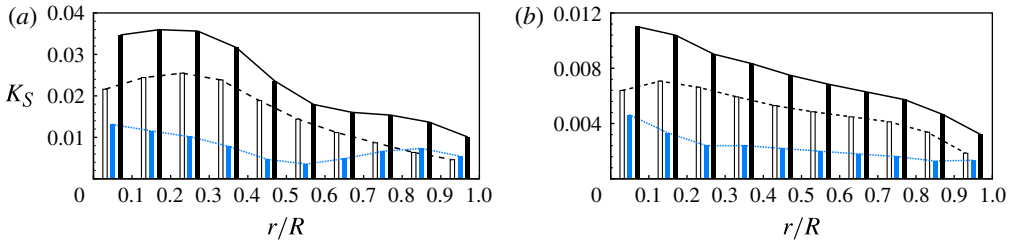

FIGURE 16. (Colour online) $J = -1.0$. Side-force magnitude loading on blade sections: - - - - - -, suction side; . . . . . ., pressure side; ——, total on blade. (*a*) w/ hull, (*b*) w/o hull.

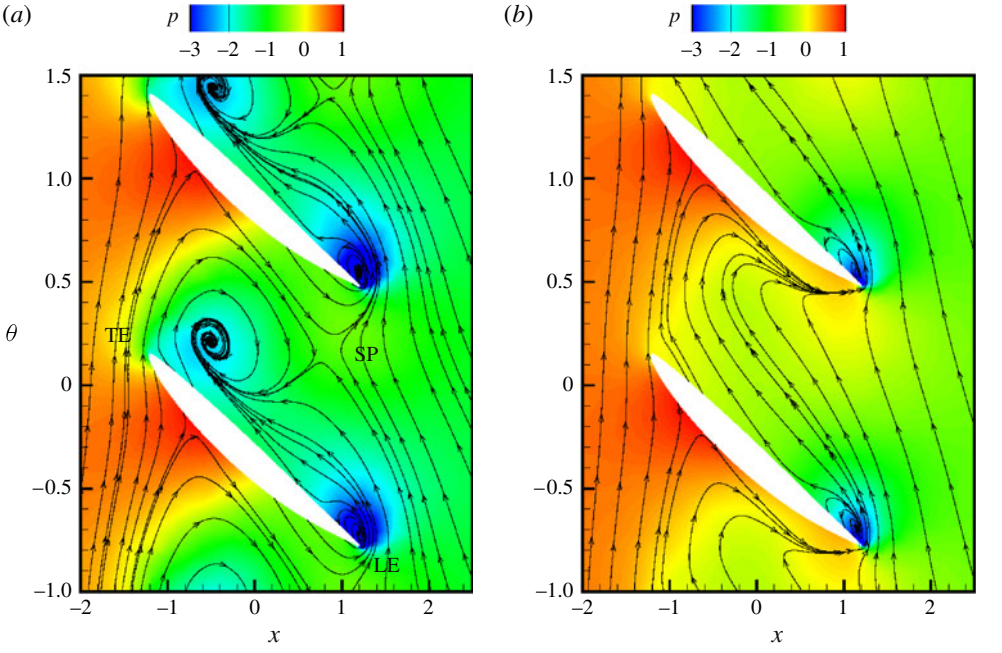

FIGURE 17. (Colour online) $J = -1.0$. Time-averaged pressure field with streamlines at a constant radial plane of $r/R = 0.4$: (*a*) w/ hull, (*b*) w/o hull.

is in contrast with the more traditional elliptical blade loading for K_T with a peak around $r/R = 0.7$.

3.3. *Mechanism of higher side force with a hull*

In order to understand the mechanism behind the generation of higher side force at the leading and trailing edge of the blades with a hull, a closer look is taken at the flow around blade sections. Figure 17 shows the time-averaged pressure field with streamlines at a constant radial plane of $r/R = 0.4$. This radial plane shows flow past blade sections, allowing an examination of the blade passage as well. Here the inflow is from left to right and propeller blades rotate in the direction of negative θ in the crashback mode. The leading and trailing edges are denoted on the figure. It is observed that the LE for the propeller with a hull (figure 17*a*) shows lower pressure

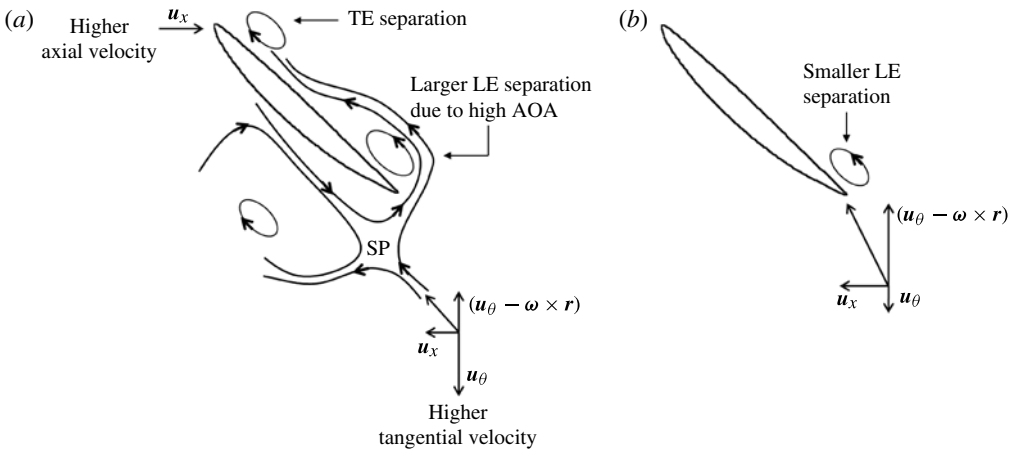

FIGURE 18. $J = -1.0$. Schematic to explain the formation of separation zones on blades near the blade root for a propeller (*a*) w/ hull, (*b*) w/o hull.

than without a hull (figure 17*b*). In fact, there is a low-pressure region even on the TE with a hull. Streamlines reveal a separation region in all these locations of low pressure.

Figure 18 is an attempt to explain the existence and formation of the separation zones near the TE and LE of the blades with a hull. It has been established earlier (in §§ 3.2.2 and 3.2.3) that the axial velocity near the blade root with a hull is greater than without a hull. This would imply a higher incoming flow towards the TE of the blade near the blade root, resulting in a TE separation zone with the hull as is seen in 17(*a*).

Even though the LE of the blade with a hull sees a lower reverse (negative) axial velocity ($\boldsymbol{u}_x$) than without hull, it does however see higher radial and tangential velocities (refer to §§ 3.2.2 and 3.2.3). The velocity vector $\boldsymbol{v}$ in the radial plane in the rotating frame of reference is formed by $\boldsymbol{v} = \boldsymbol{u}_x + (\boldsymbol{u}_\theta - \boldsymbol{\omega} \times \boldsymbol{r})$ where $\boldsymbol{\omega}$ is the rotational rate of the blades and $\boldsymbol{r}$ is the radial vector to the radial plane about the centre of rotation (propeller hub). A higher $-\boldsymbol{u}_x$, combined with lower $-\boldsymbol{u}_\theta$ makes $\boldsymbol{v}$ more akin to a backing condition inflow to the blades. This rather benign backing-type reverse inflow is what impinges on the LE of the blades without a hull, causing a small LE separation region (figure 17*b*). The reverse inflow seen by the LE of the blades with a hull deviates from this. To compound matters further, the TE separation region affects the flow pattern inside the blade passage in such a way that a saddle point (SP) is formed, figure 17*a*). The streamlines emerging from the SP appear to impinge on the LE of the blades with a hull at a very high angle of attack (AOA) leading to a larger LE separation region.

The TE separation region with a hull might serve another purpose than just to aid in the formation of a saddle point. It is probable that this separation region traps fluid within the blade passage. This confined fluid is then more likely to rotate with the blades. Evidence of this is obtained from figure 13(*a*) where the tangential velocity of the flow with a hull closely follows the tangential velocity of a blade section ($\boldsymbol{\omega} \times \boldsymbol{r}$; not shown) till $r/R < 0.5$; $\boldsymbol{\omega} \times \boldsymbol{r}$ varies linearly from $(u_\theta, r/R) \equiv (0, 0)$ to $(-1.57, 0.5)$. This implies that the tangential flow in the rotational frame of reference $(\boldsymbol{u}_\theta - \boldsymbol{\omega} \times \boldsymbol{r})$

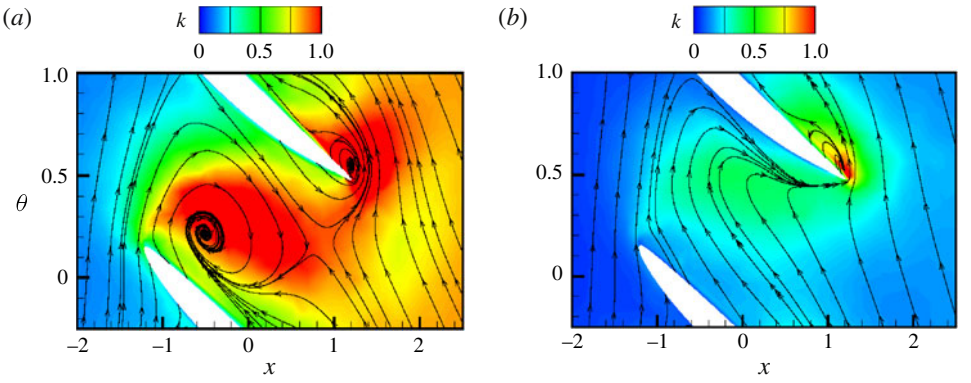

FIGURE 19. (Colour online) $J = -1.0$. Time-averaged turbulent kinetic energy field with streamlines at a constant radial plane of $r/R = 0.4$: (*a*) w/ hull, (*b*) w/o hull.

is essentially stationary in the mean. But this fluid trapped within the blade passage is still very unsteady instantaneously and leads to high turbulent kinetic energy as shown in figure 19(*a*).

To summarize, propeller blades in the presence of a hull have greater LE separation, existence of a TE separation region and possibly trapped fluid within the blade passage. LE separation directly contributes to higher side force originating on the suction and pressure side of the LE. TE separation is responsible for higher side force originating on the suction side of the TE. Higher levels of turbulent kinetic energy within the blade passage and in the near field of the blades also contributes to higher side force.

3.4. *Effect of a hull at* $J = -0.5$

Simulations were performed for the propeller with and without a hull at $J = -0.5$. $J = -0.5$ is chosen because it is higher than the critical advance ratio of $J = -0.7$ mentioned by Jessup *et al.* (2006). According to the experiments the presence of an upstream hull is not expected to make much of a difference to the performance of the propeller in crashback at this advance ratio.

3.4.1. *Time history and spectra of loads*

The time history of K_S shown in figure 20 is over 228 propeller rotations for the propeller with a hull and 214 rotations without a hull. The horizontal lines in figure 20 are $K_S \pm 1.5\sigma(K_S)$. Table 5 shows that consistently with experiments, for the current LES, the hull does not significantly affect the mean of the side-force magnitude and r.m.s. of side force at $J = -0.5$. Also the computed quantities for side force are in agreement with the experiments.

Figure 21 shows the PSD of the coefficient of side-force magnitude K_S with and without a hull. The blade passage peak at $f = 5$ rev^{-1} is again observed as it has been in previous computations and experiments. Noticeably, this peak is more prominent than at $J = -1.0$. Its magnitude is not significantly higher in the presence of the hull. A low frequency at $f = 1$ rev^{-1} is observed without the hull, similar to the LES at $J = -1.0$ and experiments (see § 3.2.1). Higher harmonics at $f = 10, 15$ rev^{-1} are also visible at this advance ratio but are significantly lower in amplitude.

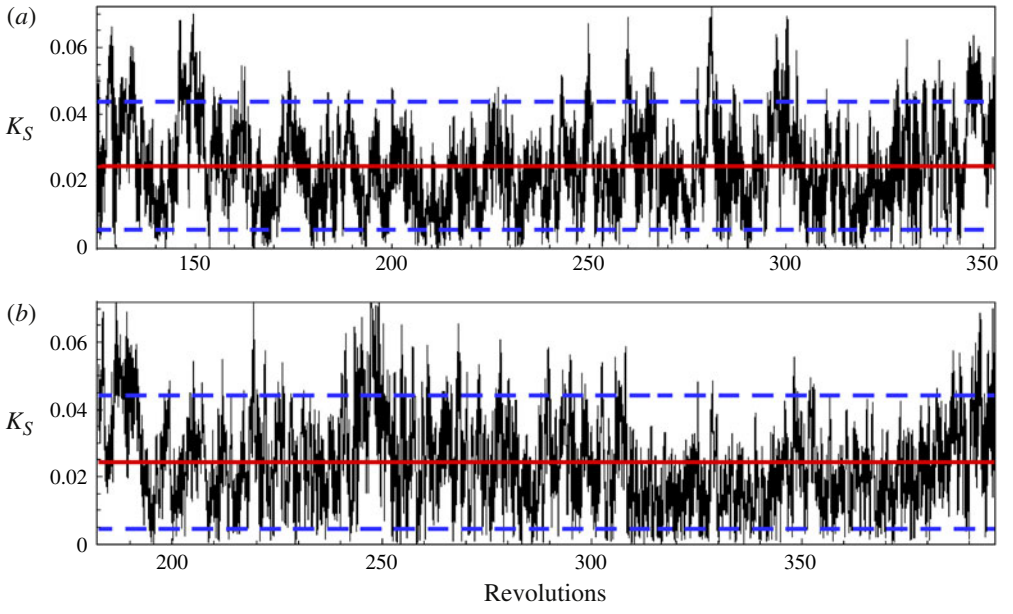

FIGURE 20. (Colour online) $J = -0.5$. Time history of unsteady loads on the propeller blades. ——, $\langle K_S \rangle$; – – – –, $\langle K_S \rangle \pm 1.5\sigma(K_S)$: (*a*) w/ hull, (*b*) w/o hull.

		$\langle K_S \rangle$	$\sigma(K_F)$	$\sigma(K_S)$
With hull	LES	0.025	0.020	0.013
	Bridges *et al.* (2008)	0.030	0.025–0.031	0.015–0.022
Without hull	LES	0.025	0.020	0.013
	Jessup *et al.* (2004)	0.025–0.033	—	0.017

TABLE 5. $J = -0.5$. Computed and experimental values of mean of side-force magnitude and r.m.s. of side force on the blades with and without a hull.

3.4.2. *Time-averaged flow field*

The time-averaged statistics shown in figure 22 are computed over 153 rotations for propeller with the hull and 200 rotations without hull. Figure 22(*a,b*) shows the time-averaged pressure contours with streamlines. Note that compared to figure 8 earlier for $J = -1.0$, there is a much smaller recirculation zone and it is located further upstream of the blades now. The vortex ring is also located closer to the blades. Figure 22(*c,d*) shows that there is only a slight radially inward displacement at the location of the centre of the vortex ring with a hull. Importantly, it is observed that the propeller blades see a higher-velocity reverse flow compared to that at $J = -1.0$ and this increased reverse flow extends from about one radius downstream of the blades to about one radius upstream.

Figure 23 shows the effect of the hull on the axial velocity profiles at $J = -0.5$. The profile in figure 23(*a*) is taken at an x-location ($x/R = -2.0$) upstream on the hull/shaft which passes through the small recirculation zone when the hull is present. Note the similarity of this profile to figure 11(*a*) which was also taken at an x-location which passed through the centre of the recirculation zone for $J = -1.0$. Figure 23(*b*)

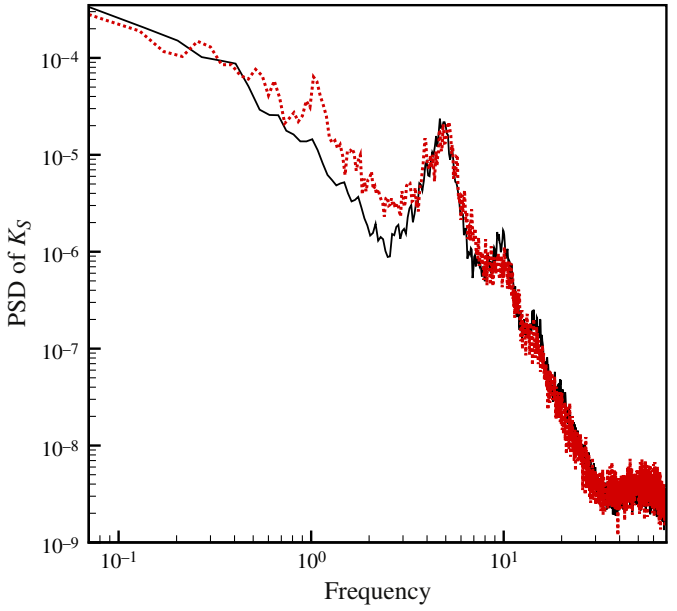

FIGURE 21. (Colour online) $J = -0.5$. PSD of K_S. ——, w/ hull; · · ·, w/o hull.

shows axial velocity profiles in the near field of the propeller blades ($x/R = -0.2$). The velocity profile for propeller with a hull at $J = -1.0$ (dash-dotted here; solid in figure 11) is also plotted along with those with and without a hull at $J = -0.5$. Note that in the near field of the blades, the hull does not make much of a difference till the blade radius ($r/R < 1$) at $J = -0.5$ and the axial velocities are much more negative than in the presence of the hull at $J = -1.0$. Compared to figure 10(a), this was not the case at $J = -1.0$ where immediately upstream of the blades, the wake of the hull interacts with the reverse flow to produce the recirculation zone. Also, looking at figure 10(a), it can be said that even without the influence of the hull, the reverse flow is not strong enough to extend upstream beyond the blades.

As has been explained earlier in § 3.3, a recirculation zone and closer vortex ring ultimately leads to greater separation on the TE and LE respectively on the suction side of the blade. At $J = -0.5$, the vortex ring is relatively close to the blades and this causes separation on the LE of the suction side leading to the low-pressure region seen in figure 24. But there is no corresponding low-pressure region on the TE with a hull and this could be attributed to the absence of the recirculation region. Since there is no TE separation, the flow inside the blade passage essentially continues along the direction of the reverse flow and does not get trapped. Figure 25 shows that at $J = -0.5$, the distribution of the pressure contribution to the side force is almost the same both with and without hull. Most of the pressure contribution to the side force comes from the LE on the suction side. The TE of the blade with a hull does not provide any higher side force as it did at $J = -1.0$.

3.5. *High- and low-amplitude events*

The propeller blades are subject to a wide range of loads during crashback. Being an off-design condition, the blades must be able to withstand extreme structural loading during the duration of this manoeuvre. Hence studying the extreme loading

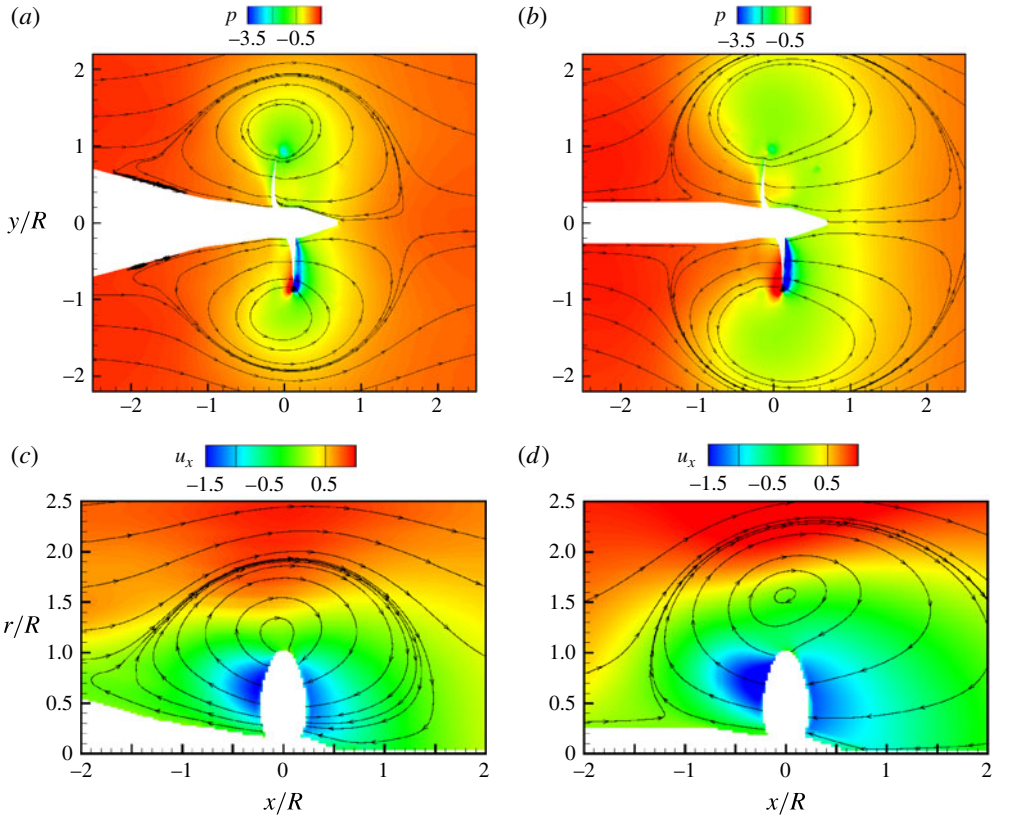

FIGURE 22. (Colour online) $J = -0.5$. Time-averaged pressure contours with streamlines (*a*) w/ hull, (*b*) w/o hull. Circumferentially averaged axial velocity with streamlines: (*c*) w/ hull; (*d*) w/o hull.

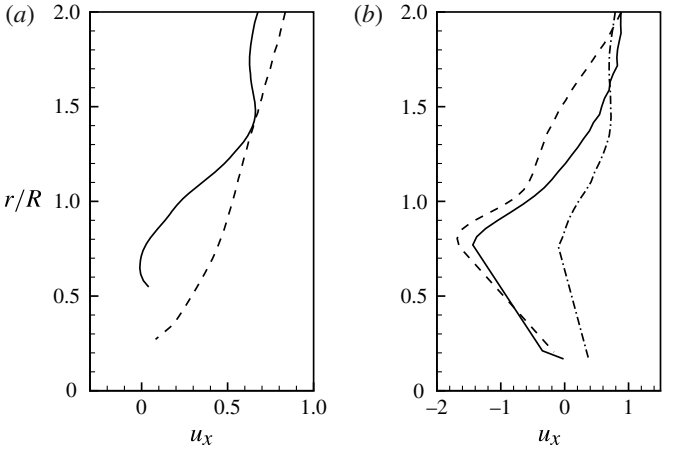

FIGURE 23. Axial velocity profiles from two x-locations upstream of the blades; $J = -0.5$: ——, w/ hull; − − −, w/o hull; $J = -1.0$: — · —, w/ hull: (*a*) $x/R = -2.0$; (*b*) $x/R = -0.2$.

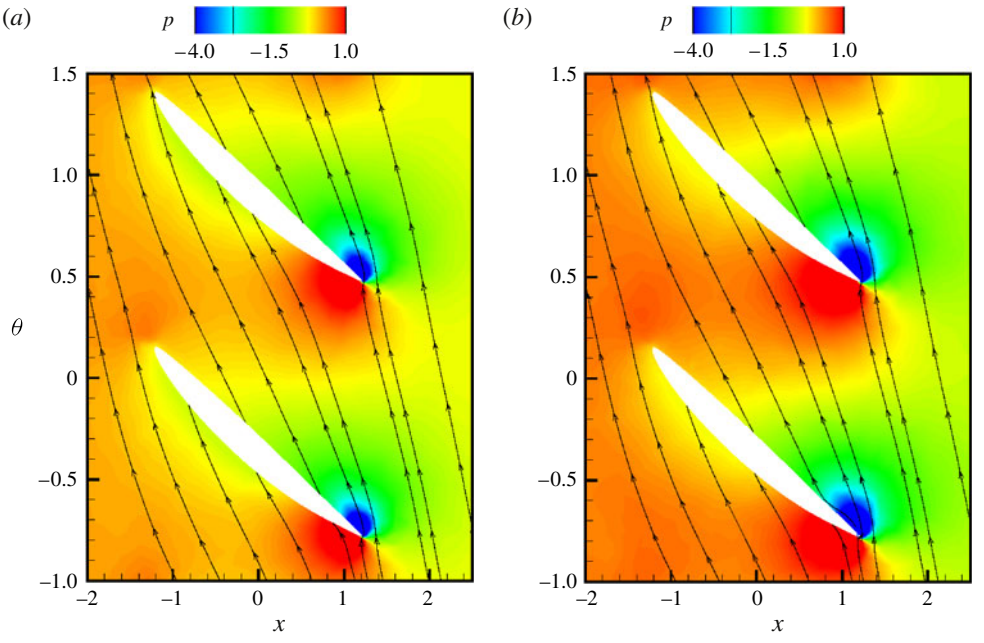

FIGURE 24. (Colour online) $J = -0.5$. Time-averaged pressure field with streamlines at a constant radial plane of $r/R = 0.4$: (*a*) w/ hull, (*b*) w/o hull.

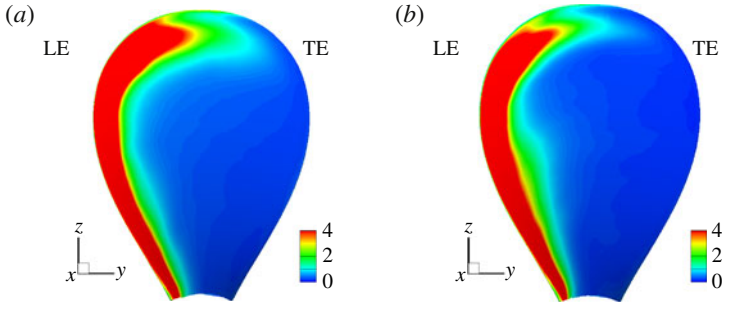

FIGURE 25. (Colour online) $J = -0.5$. Pressure contribution to the side force on the suction side (*a*) w/ hull, (*b*) w/o hull.

events is essential from the perspective of performance and structural robustness. However it is also useful in understanding the relative significance of flow features during different loading conditions. Chang *et al.* (2008) tried to explain the physics of crashback by investigating high- and low-amplitude loading events. They looked at instantaneous snapshots of the flow field during the extreme events to give a qualitative understanding of those events. Jang & Mahesh (2012) used the technique of conditional averaging (Antonia 1981) to give a more quantitative picture of the physics of crashback for a propeller without a hull during extreme loading events. Conditionally sampled flow fields are analysed in the current subsection to reveal the

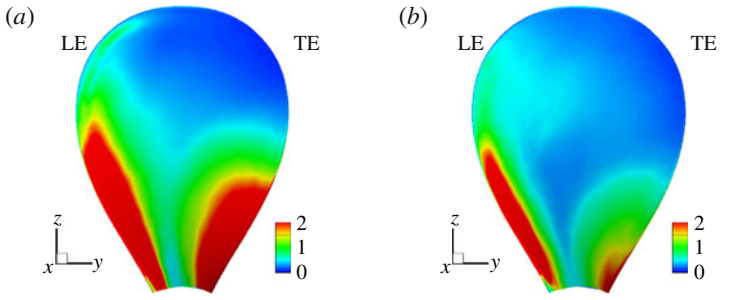

FIGURE 26. (Colour online) $J = -1.0$. Pressure contribution to side force w/ hull on suction side during: (*a*) high K_S; (*b*) low K_S.

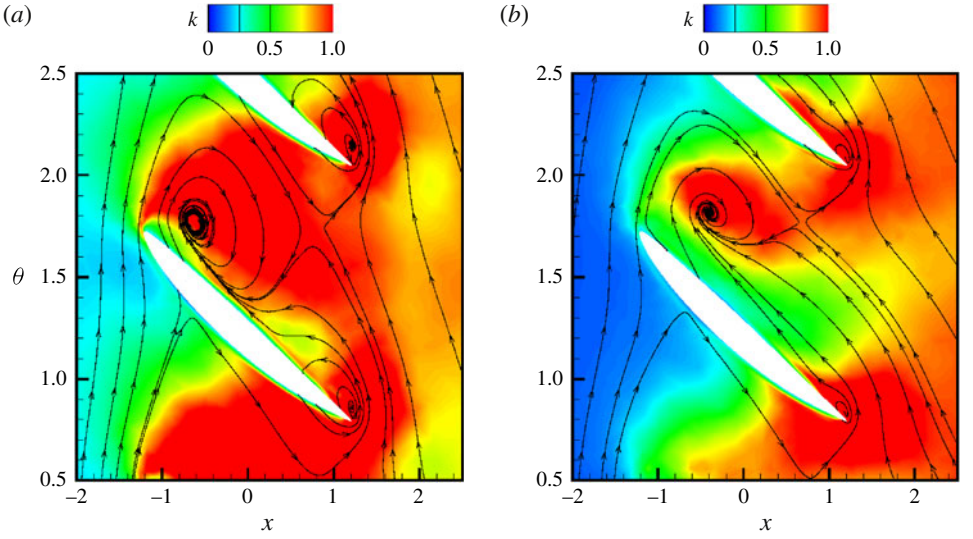

FIGURE 27. (Colour online) $J = -1.0$. Turbulent kinetic energy field with streamlines at a constant radial plane of $r/R = 0.4$ w/ hull during (*a*) high K_S; (*b*) low K_S.

impact of the recirculation region and vortex ring on production of extreme thrust and side force in the presence of a hull at $J = -1.0$ and $J = -0.5$.

Firstly, the flow field is conditionally averaged at $J = -1.0$ for the case with a hull for $K_S \pm 1.5\sigma(K_S)$ to represent high- and low-side-force events. Time-averaged conditional statistics of the flow field are computed over 65 propeller rotations, which is included in the time window for which the time history of K_S is shown in figure 6(*a*). Figure 26 shows that the location of generation of higher side force during high-K_S events is consistent with figure 15. Though not shown here, the pressure-side LE has a slightly higher contribution during high-K_S events but most of the side force originates from the suction side.

Noticeably, the TE of the suction side plays a greater role during high-K_S events. This points towards greater TE separation leading to higher TE unsteadiness as shown in figure 27. Also note the higher LE unsteadiness, as is to be expected during high-K_S events. Greater TE separation in the presence of a hull at $J = -1.0$ was ascribed

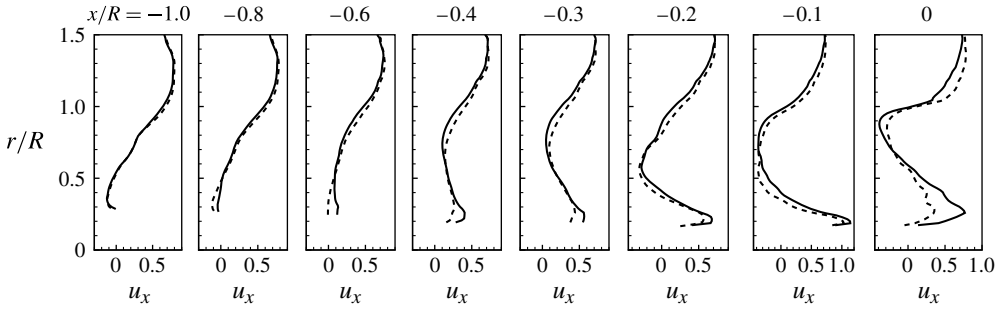

FIGURE 28. $J = -1.0$. Circumferentially averaged axial velocity profiles from eight x-locations leading up to the blades w/ hull. ——, high K_S; – – – –, low K_S.

	x_{cen}/R	r_{cen}/R
High K_S	−1.101	0.549
Low K_S	−0.996	0.529

TABLE 6. $J = -1.0$. Location of centre of recirculation region w/ hull during: (a) high K_S, (b) low K_S.

to higher axial velocity near the blade root in § 3.2.3. That assertion is re-affirmed through figure 28 which shows the axial velocity profiles at different x-locations leading up to the blade. The axial velocity during high-K_S events is always higher below $r/R = 0.5$. It is believed that a slightly upstream recirculation region allows the flow to accelerate through a larger axial distance to cause a higher axial velocity in the near field of the propeller blades. Table 6 shows that the recirculation region is located slightly further upstream (x_{cen}/R is smaller) and is also slightly bigger in size (r_{cen}/R is greater) during high-K_S events. Lower side force originating from the suction-side LE during low-K_S events is due to smaller LE separation which is consistent with greater reverse flow (which reduces the angle of attack as shown in § 3.3). This greater reverse flow during low-K_S events is also apparent from figure 28 at $x/R = 0$. In fact, the TE is also responsible for higher K_T during high-K_S events. It can be concluded that the recirculation region near the inflow of the propeller blades plays a greater role in generation of high forces at $J = -1.0$.

The flow field was conditionally averaged at $J = -0.5$ for the case with a hull. At this advance ratio, thrust and side force are correlated. More particularly, high- and low-thrust events are correlated with high- and low-side-force events respectively, as also observed by Jang & Mahesh (2012). To demonstrate that this is also the case with a hull, results are shown with conditionally averaging at $J = -0.5$ with a hull for $K_T \pm 1.5\sigma(K_T)$ to represent high- and low-thrust events over 47 propeller rotations, which is included in the time window for which the time history of K_S is shown in figure 20(a). Figure 29 shows that both the thrust and side force are higher during the high-K_T events when compared with the low-K_T events. Consistently, most of the side force is generated from the LE of the suction side and hence is attributable to greater LE separation.

There is a very small recirculation region far upstream on the hull during high K_T (figure 30) located at $x_{cen}/R = -2.15$. During low K_T, it is almost absent and could be

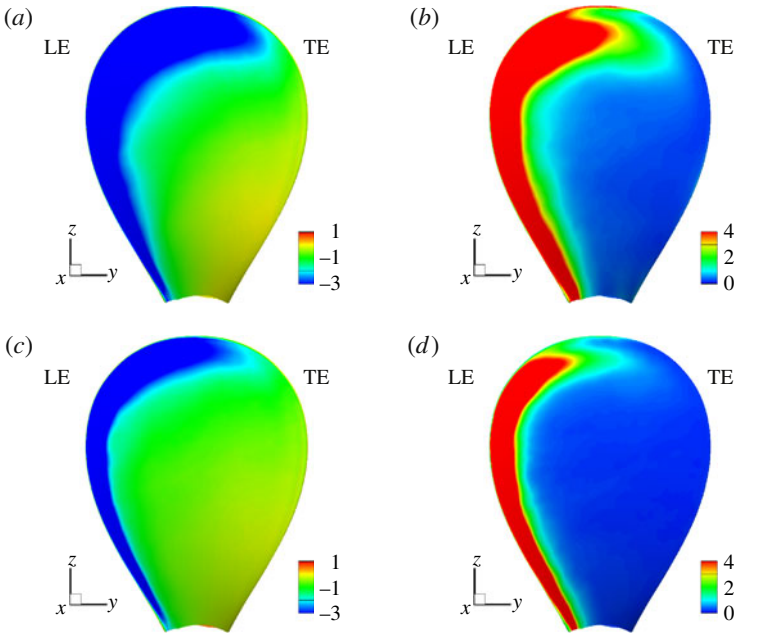

FIGURE 29. (Colour online) $J = -0.5$. Pressure contribution to thrust and side force w/ hull on the suction side during: high K_T (*a*) thrust, (*b*) side force; low K_T (*c*) thrust, (*d*) side force.

	$J = -1.0$	$J = -0.5$
High K_T	0.988	1.178
Low K_T	1.009	1.268

TABLE 7. Distance of centre of vortex ring from the centre of the propeller w/hull during high and low K_T events at $J = -1.0$ and $J = -0.5$.

located further upstream at $x_{cen}/R = -2.75$. But even during high K_T, the recirculation region is too far upstream to have any effect near the TE of the blade root as it does at $J = -1.0$. As expected from the absence of appreciable side force generated from the TE on the suction side of the blade, there is no noticeable TE separation. It can be concluded that the recirculation region does not impact on the flow in the near field of the propeller blades at $J = -0.5$.

Figure 30(*a*,*b*) also shows that for high K_T, the centre of the vortex ring is located closer to the tip of the propeller blades as listed in table 7. Higher unsteadiness is observed near the tip and LE of the blade (figure 30*c*) which translates into relatively higher forces near the blade tip during high-K_T (and K_S) events. Thus proximity of the vortex ring to the propeller blades plays a greater role in generation of higher forces at this advance ratio.

Table 7 also shows that the vortex ring is closer at $J = -1.0$ than at $J = -0.5$. However, there is only a slight difference between high and low K_T at $J = -1.0$. This re-affirms that even though a closer vortex ring will lead to higher forces at any advance ratio, it is not as dominant a mechanism of force generation at $J = -1.0$ as

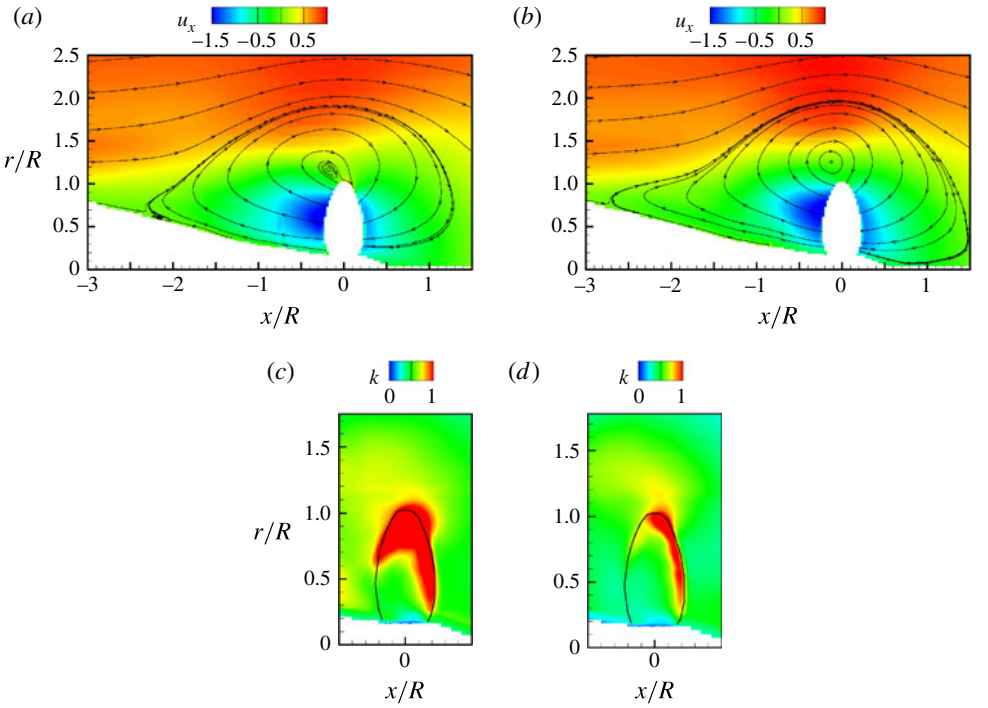

FIGURE 30. (Colour online) $J = -0.5$. Circumferentially averaged field w/hull: axial velocity with streamlines for (*a*) high K_T, (*b*) low K_T; turbulent kinetic energy for (*c*) high K_T, (*d*) low K_T.

it is at $J = -0.5$. This can also be gauged by observing that the outboard half of the blade is not the major contributor to side force at $J = -1.0$.

4. Mechanism of different side force at different advance ratios with a hull

The above results suggest the following model to explain the mechanism of different side force at different advance ratios (figure 31). At lower negative advance ratio, such as $J = -0.5$, the higher rotational rate of the propeller blades causes a higher reverse flow into the blades. Higher reverse flow is closer to an attached-flow-like condition and hence LE separation is small compared to $J = -1.0$. This reverse flow also interacts with the hull at a greater upstream distance from the propeller, thus suppressing the recirculation zone. Velocities upstream of the blades are still high enough and so the vortex ring does not form too close to the blades as expected, with the hull. As a result, the hull does not make much of a difference to the flow in the near field of the blades when the propeller rotation rate is higher, which is same as a lower negative advance ratio. Hence results with and without a hull are very similar at $J = -0.5$.

On the other hand, at a higher negative advance ratio such as $J = -1.0$, the reverse flow is not high enough. This causes larger LE separation compared to $J = -0.5$ and a recirculation zone forms upstream of the blades with the hull. The close recirculation region accelerates the flow approaching the blades from the pressure side. This causes a closer vortex ring but, much more importantly, TE separation near the root of the blade. The near field of the blades is affected to the extent of causing higher side force at a higher negative advance ratio.

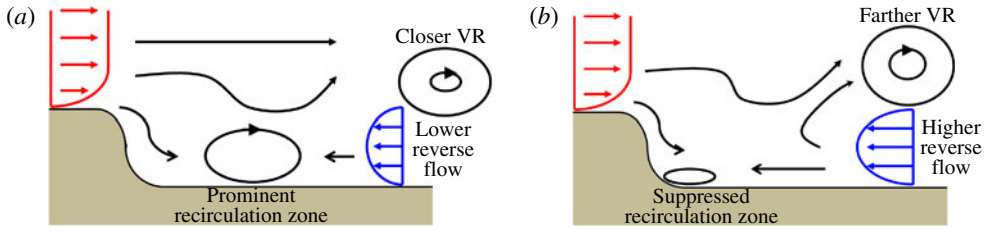

FIGURE 31. (Colour online) $J = -0.5$. Schematic to explain flow in the presence of a hull at (*a*) high negative advance ratio ($J = -1.0$); (*b*) low negative advance ratio ($J = -0.5$). VR denotes vortex ring.

5. Conclusion

Crashback simulations for a propeller with and without a hull have been performed at the advance ratios $J = -0.5$ and $J = -1.0$. According to Bridges' experiment (Bridges 2004) with an upstream hull, side force increase dramatically as J is reduced below -0.7. At both advance ratios, computed mean, r.m.s. and spectra of side force show reasonable agreement with the experimental data for both with and without the hull. At $J = -1.0$, two new noticeable flow features are found with the hull. A recirculation zone is found to exist upstream of the propeller blades and the centre of the vortex ring is located much closer to the blades. The presence of the recirculation zone decreases the momentum of the flow which causes the vortex ring to be located closer to the blades. The recirculation zone and the closer vortex ring alter the flow in the near field of the propeller blades with a hull. At $J = -0.5$, the upstream recirculation zone with the hull is suppressed because the reverse flow from propeller rotation is higher and there is not much difference in the location of the vortex ring with and without a hull. The pressure contribution to the side force with a hull is significantly higher than without a hull at $J = -1.0$. For both advance ratios, the side force with a hull is mainly generated from leading-edge separation on the suction side. However, at $J = -1.0$, higher side force is also generated from trailing-edge separation on the suction side. At $J = -1.0$, propeller blades with a hull have greater LE separation, existence of a TE separation region and possibly trapped fluid within the blade passage. LE separation directly contributes to higher side force originating on the suction and pressure sides of the LE. TE separation is responsible for higher side force originating on the suction side of the TE. Higher levels of turbulent kinetic energy within the blade passage and in the near field of the blades also contributes to higher side force. At low negative advance ratios ($J = -0.5$), the vortex ring is the dominant flow feature affecting blade forces through the suction-side LE. At high negative advance ratios ($J = -1.0$), the recirculation region is an additional and more dominant flow feature increasing blade forces through the suction-side TE.

Acknowledgements

This work was supported by the United States Office of Naval Research under ONR Grant N00014-05-1-0003 with Dr K.-H. Kim as technical monitor. Computing resources were provided by the Arctic Region Supercomputing Center of HPCMP and the Minnesota Supercomputing Institute. We are grateful to Dr M. Donnelly, Dr S. Jessup and their colleagues at NSWCCD for providing us with experimental data.

REFERENCES

ANTONIA, R. A. 1981 Conditional sampling in turbulence measurement. *Annu. Rev. Fluid Mech.* **13**, 131–156.

BRIDGES, D. H. 2004 A detailed study of the flow field of a submarine propeller during a crashback maneuver. *Tech Rep.* MSSU-ASE-04-1. Department of Aerospace Engineering, Mississippi State University.

BRIDGES, D. H., DONNELLY, M. J. & PARK, T. J. 2008 Experimental investigation of the submarine crashback maneuver. *Trans. ASME: J. Fluids Engng* **130**.

CHANG, P., EBERT, M., YOUNG, Y. L., LIU, Z., MAHESH, K., JANG, H. & SHEARER, M. 2008 Propeller forces and structural responses to crashback. In *Proceedings of the 27th Symposium on Naval Hydrodynamics, Seoul, Korea*, vol. 2, pp. 1069–1091. Curran Associates.

CHEN, B. & STERN, F. 1999 Computational fluid dynamics of four quadrant marine propeller flow. *J. Ship Res.* **43** (4), 218.

DAVOUDZADEH, F., TAYLOR, L. K., ZIERKE, W. C., DREYER, J. J., MCDONALD, H. & WHITFIELD, D. L. 1997 Coupled Navier–Stokes and equations of motion simulation of submarine maneuvers, including crashback. In *Proceedings of the 1997 ASME Fluids Engineering Division Summer Meeting, New York*.

GERMANO, M., PIOMELLI, U., MOIN, P. & CABOT, W. H. 1991 A dynamic subgrid–scale eddy viscosity model. *Phys. Fluids* A **3** (7), 1760.

GREEN, R. B., GILLIES, E. A. & BROWN, R. E. 2005 The flow field around a rotor in axial descent. *J. Fluid Mech.* **534**, 237–261.

JANG, H. & MAHESH, K. 2012 Large eddy simulation of flow around a reverse rotating propeller. *J. Fluid Mech.* (submitted).

JESSUP, S., CHESNAKAS, C., FRY, D., DONNELLY, M., BLACK, S. & PARK, J. 2004 Propeller performance at extreme off design conditions. In *Proceedings of the 25th Symposium on Naval Hydrodynamics, St John's, Canada*.

JESSUP, S., FRY, D. & DONNELLY, M. 2006 Unsteady propeller performance in crashback conditions with and without duct. In *Proceedings of the 26th Symposium on Naval Hydrodynamics, Rome, Italy*.

JIANG, C. W., DONG, R. R., LUI, H. L. & CHANG, M. S. 1997 24–inch water tunnel flow field measurements during propeller crashback. In *Proceedings of the 21st Symposium on Naval Hydrodynamics*. The National Academies Press.

LE, H., MOIN, P. & KIM, J. 1997 Direct numerical simulation of turbulent flow over a backward–facing step. *J. Fluid Mech.* **330**, 349–374.

LILLY, D. K. 1992 A proposed modification of the germano subgrid–scale closure model. *Phys. Fluids* A **4** (3), 633.

MAHESH, K., CONSTANTINESCU, G. & MOIN, P. 2004 A numerical method for large–eddy simulation in complex geometries. *J. Comput. Phys.* **197** (1), 215.

VYŠOHLID, M. & MAHESH, K. 2006 Large eddy simulation of crashback in marine propellers. In *Proceedings of the 26th Symposium on Naval Hydrodynamics, Rome, Italy*, vol. 2, pp. 131–141.